System Modeling and Control Strategy of a Superconducting Powertrain for Electric Aircraft

Ali Khonya, Mathias Noe, Frederick Berg, Lars Kühn, Reda Abdouh, Wescley T. B. de Sousa, Alexandre Colle, Michael Cooper

***Abstract*—Aviation contributes approximately 2.4% to the annual global CO_2 emissions. This serves as a driving force behind the development of a fully electric, zero-emission aircraft. One possibility is using liquid hydrogen at a temperature of 20 K that fits very well with lightweight and efficient superconducting components within an electric aircraft to produce energy through a fuel cell, as it has the highest energy content per weight among all energy carriers. A potential powertrain of a large electric aircraft comprises various components, including the motor, DC/AC inverter, DC and AC cables, fuel cell, and fault current limiter. Building on previous work that modeled superconducting fault current limiters and cables using MATLAB/SIMULINK, this study focuses on the motor, DC/AC inverter, and fuel cell. For the fuel cell, even though most publications propose only the resistive-capacitive (R-C) electrical equivalent circuit, in some cases, a resistive-inductive (R-L) behavior or sometimes a combination of both is detected. Therefore, a novel model that covers all scenarios is proposed for this work. Furthermore, the electrical model and control scheme of the permanent magnet synchronous motor (PMSM) via a DC/AC inverter are detailed. Additionally, an algorithm is developed to protect the inverter during short circuits. The simulation flight scenarios are employed with input speed as a key parameter to simulate the complete integrated system. Moreover, a DC pole-to-pole short circuit is analyzed to simulate the system's behavior in fault conditions. The simulation shows the entire system's behavior during nominal test flight scenarios and short circuit events. Moreover, these models give the user flexibility to adjust the powertrain properties.**

***Index Terms*—Electric Aircraft, Superconducting Powertrain, Polymer Exchange Membrane Fuel Cell, Motor Control.**

I. Introduction

AVIATION has been under investigation in recent years to tackle its 2.4% of the annual CO_2 emissions challenge [1], [2]. With 85% of these emissions coming from passenger flights and a projected yearly passenger traffic growth of 3.6-6.8%, air travel carbon emissions are expected to double by 2050 [3], [4]. Previous research works show that to achieve the net zero target, the most feasible solutions are sustainable aviation fuel (SAF) and green hydrogen [5], [6]. Despite SAF, which can only be burnt in combustion engines, green hydrogen can be used in both combustion engines or to produce electricity through fuel cell stacks [5]. In this work, an electric aircraft with hydrogen as energy carrier and the fuel cell as energy generation is investigated in combination with lightweight and efficient superconducting components within the whole powertrain [7]. Considering all the benefits and the motivation for an electric aircraft with a superconducting powertrain, a model to simulate the entire system in a power simulator tool like MATLAB SIMULINK is pivotal. This work focuses on providing the approach for such a model, which should be adjustable and adaptable under various requirements, providing accurate results to simulate the powertrain behavior and sizing estimation of the components.

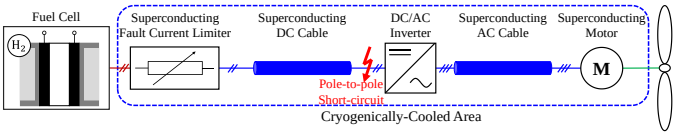

Fig. 1. Schematic of the electric aircraft superconducting powertrain [8].

TABLE I
Main Specifications Considered for the Electric Aircraft Powertrain.

Parameter	Symbol	Value
Maximum DC power (total power)	$P_{\max}$	456 kW
Maximum speed	$n_{\max}$	1043 rpm
Maximum nominal AC current	$I_{\mathrm{AC,nom}}$	1.8 kA
Minimum nominal pole-to-pole DC voltage	$U_{\mathrm{DC,nom}}$	300 V
Maximum nominal DC current	$I_{\mathrm{DC,nom}}$	1.52 kA

A potential superconducting powertrain architecture for an electric aircraft is shown in Fig. 1, with the basic specifications described in TABLE I [8]. In this system, the superconducting bipolar DC and three-phase AC cables are used to transport energy from the fuel cell stacks to the permanent magnet synchronous motor (PMSM). The torque and the speed of the PMSM are controlled by a DC/AC inverter via field-oriented control (FOC), as the most well-known technique method. Moreover, a resistive superconducting fault current limiter (RSFCL) limits current rises in the system. For this study, liquid nitrogen (LN_2) at a temperature of 77 K is the cooling medium for the system. Previously in [8], modeling of the RSFCL and cables in MATLAB/SIMULINK with the properties described in TABLE II made up of REBCO tapes was explained, and the focus in this work is on the DC/AC inverter, motor, and fuel cell. Finally, the complete system is simulated in SIMULINK under different scenarios.

II. Fuel Cell

The fuel cell, as an electrochemical system converting chemical energy into electrical energy, generally consists of

A. Khonya, M. Noe, and W. De Sousa are with Institute for Technical Physics, Karlsruhe Institute of Technology, Karlsruhe, Germany

F. Berg, L. Kühn, and M. Cooper are with Airbus X-Labs, Taufkirchen, Germany, and R. Abdouh and A. Colle are with Airbus UpNext, Toulouse, France.

TABLE II
PROPERTIES OF THE RSFCL, BIPOLAR DC CABLE, AND THREE-PHASE AC CABLE [8].

Parameter	RSFCL	DC Cable	AC Cable
Number of tapes	3 tapes	8 tapes in inner pole 12 tapes in outer pole	8 layers/phase 3 tapes/layer
Tapes critical current / A	550	210	100
Tapes length / m	8.5	50	2.4
Inductance / μH	-	6.91	0.89

TABLE III
FUEL CELL UNIT AND STACK PROPERTIES [12].

Parameter	Symbol	Value
Membrane thickness	l_{M}	178 μm
Fuel cell unit active area	A_{FC}	64 cm^2
Cell operating temperature	T	333 K
Hydrogen pressure	$p_{\mathrm{H_2}}$	1 atm
Oxygen pressure	$p_{\mathrm{O_2}}$	0.2095 atm
Fuel cell maximum current density	$J_{\mathrm{FC,max}}$	0.469 A/cm^2
Number of cells in the stack	N_{c}	500
Stack active area	$A_{\mathrm{FC,st}}$	0.385 m^2

two electrodes, cathode and anode, and an electrolyte membrane in the middle [9]. Depending on the electrolyte material and chemical reactions inside the fuel cell, there are several types of fuel cell systems such as Proton Exchange Membrane Fuel Cell (PEMFC), Alkaline Fuel Cell (AFC), and Phosphoric Acid Fuel Cell (PAFC) [10]. This work considers PEMFCs as they are particularly well-suited for aeronautic applications due to the high efficiency and fast startup [11].

A. Fuel Cell Stack Design

This work considers a fuel cell unit based on [12] with the properties described in TABLE III. To design a stack of fuel cells, based on the system requirements given in TABLE I, the voltage-current characteristic named the fuel cell polarization curve is needed. In a PEMFC, the thermodynamic potential of a unit cell that represents its voltage is called Nernst potential, shown with E_{Nernst}. This voltage, which varies with the cell temperature and hydrogen and oxygen pressures, is calculated with (1) [12].

$$\begin{aligned} E_{\mathrm{Nernst}} &= 1.229 - 0.85 \times 10^{-3}(T - 298.15) \\ &\quad + 4.31 \times 10^{-5} T \cdot [\ln(p_{\mathrm{H_2}}) + 0.5 \ln(p_{\mathrm{O_2}})] \end{aligned} \tag{1}$$

Nernst potential is an ideal voltage a PEMFC can generate, but the output voltage is lower due to the different voltage drops inside the fuel cell unit. These voltage drops are [13]:

- activation voltage drop (u_{act}): due to the electrodes activation to initiate a chemical reaction between reactants
- Concentration voltage drop (u_{con}): due to the change in the reactants concentration at the surface of the electrodes
- Ohmic voltage loss (u_{Ω}): due to the membrane resistance to the electron flow and the electrodes contact resistance

Calculation of these voltage drops is found in [12]–[14]. The fuel cell unit output voltage u_{FC} is then calculated with (2).

$$u_{\mathrm{FC}} = E_{\mathrm{Nernst}} - u_{\mathrm{act}} - u_{\mathrm{con}} - u_{\Omega} \tag{2}$$

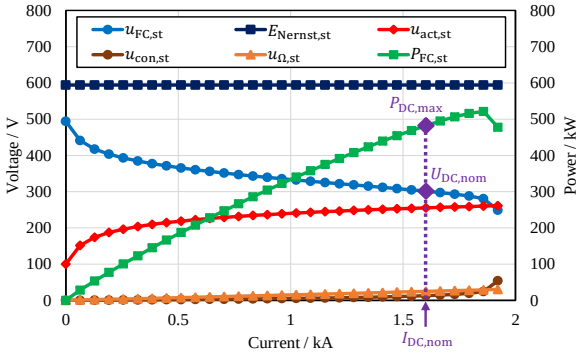

Fig. 2. Fuel cell stack polarization curve.

Based on the cell polarization curve, the nominal operating point for the stack design is chosen as (3).

$$J_{\mathrm{FC,nom}} = 0.375\mathrm{mA/cm^2}, U_{\mathrm{FC,nom}} = 0.6\mathrm{V}, P_{\mathrm{FC,nom}} = 14.4\mathrm{W} \tag{3}$$

The required number of cells in the stack N_{c} is calculated based on the minimum nominal DC voltage provided in TABLE I and nominal voltage of a single cell unit using (4).

$$N_{\mathrm{c}} = \frac{U_{\mathrm{DC,nom}}}{U_{\mathrm{FC,nom}}} \tag{4}$$

Moreover, to deliver the required power $P_{\mathrm{DC,max}}$, the stack active area $A_{\mathrm{FC,st}}$ is adjusted based on the maximum current $I_{\mathrm{DC,nom}}$ and nominal current density $J_{\mathrm{FC,nom}}$ with (5).

$$A_{\mathrm{FC,st}} = \frac{I_{\mathrm{DC,nom}}}{J_{\mathrm{FC,nom}}} = \frac{P_{\mathrm{DC,max}}}{U_{\mathrm{DC,nom}} \cdot J_{\mathrm{FC,nom}}} \tag{5}$$

The stack design parameters are given in TABLE II, and its polarization curve is illustrated in Fig. 2. In this figure, the cell stack power $P_{\mathrm{FC,st}}$ is calculated from its voltage $u_{\mathrm{FC,st}}$ and current $i_{\mathrm{FC,st}}$ with (6).

$$P_{\mathrm{FC,st}} = u_{\mathrm{FC,st}} \cdot i_{\mathrm{FC,st}} \tag{6}$$

B. Fuel Cell Electrochemical Model

As shown in Fig. 2, the fuel cell voltage varies with the change in the fuel cell current. This variation is not immediate, and it takes time for the fuel cell to reach its steady-state condition. Most studies propose a resistive-capacitive (R-C) electrical equivalent circuit to model the PEMFC behavior [12]–[16]. However, a resistive-inductive (R-L) behavior equivalent circuit is detected in some works [17]–[20]. In addition, a fuel cell system might not exhibit purely resistive-capacitive or resistive-inductive behavior when its current changes and it could include characteristics of both. As indicated in multiple studies, such as [18] and [20], an R-L behavior is observed when the current increases, whereas an R-C response is detected when the current decreases. The simulation model considers normal operation and transient conditions and allows the user to select the desired behavior. The R-C and R-L equivalent circuits of the fuel cell stack are depicted in Fig. 3., where the index "st" stands for the stack,

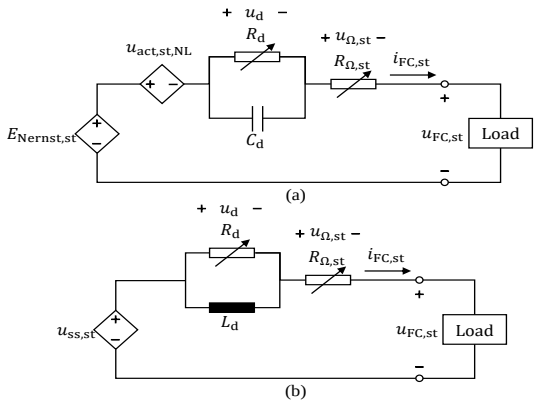

Fig. 3. Fuel cell stack equivalent circuits: (a) resistive-capacitive equivalent circuit, (b) resistive-inductive equivalent circuit.

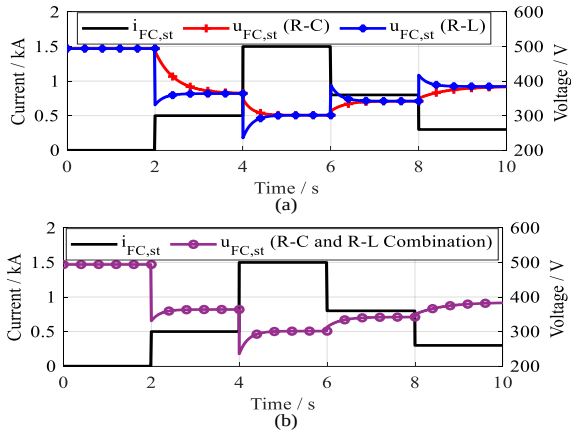

Fig. 4. Fuel cell stack simulation results considering: (a) resistive-capacitive or resistive-inductive behaviors, (b) combination of the resistive-capacitive (current decrease) and resistive-inductive (current increase) behaviors.

$u_{ac,st,NL}$ represents the stack activation voltage drop at no-load condition ($i_{FC,st}$=0A), and $u_{ss,st}$ is the steady-state stack voltage which is calculated with (7).

$$u_{ss,st} = E_{Nernst,st} - u_{act,st} - u_{con,st} \tag{7}$$

Furthermore, to model the fuel cell dynamic behavior, an R-C or R-L branch is implemented in the circuits, with R_d, C_d, and L_d indicating the dynamic resistance, capacitance, and inductance. These parameters are chosen based on the dynamic behavior such as the time to reach the steady-state condition.

C. Fuel Cell Simulation

A PEMFC model considering the possible dynamic behaviors (chosen by the user) is developed in MATLAB SIMULINK. In a study case, the load current $i_{FC,st}$ varies in a 10 s interval with 1 s steps between 0 A to 1.5 kA. The results are demonstrated in Fig. 4 assuming approximately 1 s for the fuel cell to reach its steady-state condition. With the combined R-C and R-L models, the simulation result shown in Fig. 4(b) gives more realistic results in some cases compared to the experiments within the literature [18], [20].

TABLE IV
SUPERCONDUCTING MOTOR PARAMETERS.

Parameter	Symbol	Value
Number of pole pairs	N_{pp}	6
Stator resistance	R_s	10 $\mu\Omega$
Stator (d- and q-axis) inductance	L_s=L_d=L_q	8.5 μH
Permanent magnet flux linkage	φ_{PM}	0.2577 Wb
Nominal (maximum) torque	T_{max}	4175 N.m
Propeller inertia	J	0.1176 kg·m^2
Propeller damping coefficient	B	38.25 N·m/(rad/s)

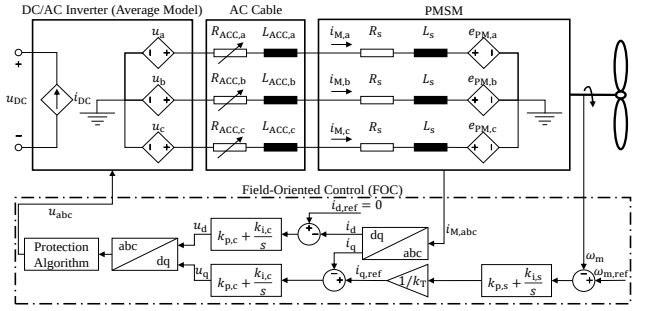

Fig. 5. PMSM, superconducting AC cable, and DC/AC inverter electrical equivalent circuit with the FOC schematic of the PMSM.

III. DC/AC Inverter and Superconducting Motor

A. Inverter and Motor Electrical Model

A permanent magnet synchronous motor (PMSM) with a stator made up of superconducting tapes with the parameters described in TABLE IV is considered in this work. In nominal conditions, a PMSM can be treated like a conventional motor, with the difference of having a significantly small stator resistance (10 $\mu\Omega$) due to the superconducting materials.

Figure. 5 illustrates the electrical equivalent circuits of the PMSM and superconducting AC cable (ACC). The parameters $R_{ACC,abc}$ (approximately zero in nominal conditions) and $L_{ACC,abc}$ (given in TABLE II) represent the phase resistance and inductance of the superconducting AC cable. Moreover, since the switching effects of the inverter are neglected, this work considers an average model of the inverter. Furthermore, in the PMSM circuit, $e_{PM,abc}$ is the three-phase back electromotive force (EMF) generated by the permanent magnet (PM). This EMF is assumed to vary sinusoidally over time t and is determined by mechanical speed ω_m, number of pole pairs N_{pp} and PM flux linkage φ_{PM} with (8). The three-phase angles θ_{abc} in (8) are given as θ_a=0, θ_b=2π/3, and θ_c=4π/3.

$$e_{PM,abc} = \varphi_{PM} \cdot N_{pp} \cdot \omega_m \cdot \sin(N_{pp} \cdot \omega_m \cdot t + \theta_{abc}) \tag{8}$$

B. Motor Control

The field-oriented control (FOC) is the most well-known and adaptable PMSM control technique, offering a stable control with reduced ripple, fast dynamic response, and high control accuracy [21], [22]. The PMSM FOC schematic via inverter is depicted in Fig. 5. In this method, the motor currents $i_{M,abc}$ are converted to the dq-axis using Park transform (abc to dq0) [21]. To optimize the electromagnetic torque T_e, the reference motor current in the d-axis i_d is set to zero, while

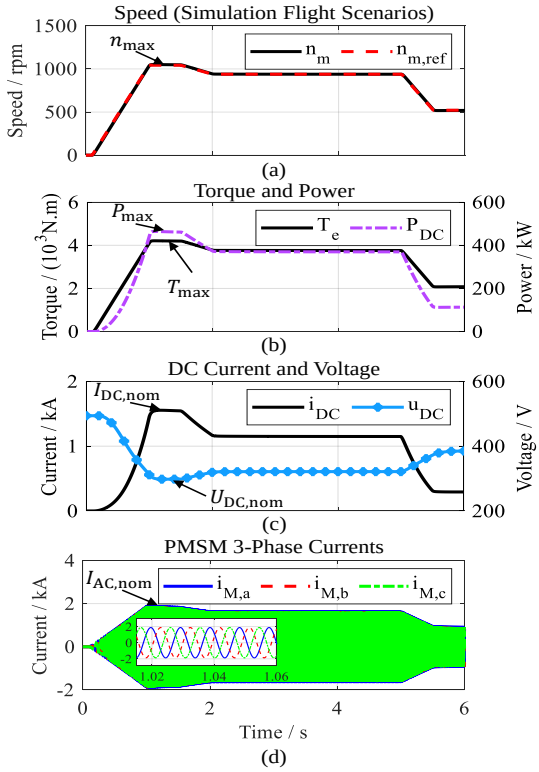

Fig. 6. Simulation flight scenarios simulation results: (a) speed as the input scenario with $n_{\mathrm{m,ref}}$ being the reference speed and n_{m} as the actual speed resulting from the motor control, (b) torque and total (DC) power, (c) DC current and voltage on the fuel cell output, (d) PMSM three-phase currents.

the q-axis current i_{q} is maximized. The relationship between T_{e} and i_{q} is given in (9), with k_{T} as the torque constant.

$$T_{\mathrm{e}} = 1.5 N_{\mathrm{pp}} \cdot \varphi_{\mathrm{PM}} \cdot i_{\mathrm{q}} = k_{\mathrm{T}} \cdot i_{\mathrm{q}} \tag{9}$$

From torque T_{e}, the actual motor speed ω_{m} is calculated using the torque balance equation described in (10).

$$T_{\mathrm{e}} = T_{\mathrm{L}} + B \cdot \omega_{\mathrm{m}} + J \cdot \frac{d\omega_{\mathrm{m}}}{dt} \tag{10}$$

In the FOC, the tuning of the PI controllers is based on the desired response speed and the transient error. The current controller parameters, $k_{\mathrm{p,c}}$ and $k_{\mathrm{i,c}}$, are adjusted based on the stator inductance L_{s} and resistance R_{s}. Similarly, the speed controller parameters $k_{\mathrm{p,s}}$ and $k_{\mathrm{i,s}}$ are tuned according to the rotor inertia J and friction B. Additionally, an algorithm is developed to protect the inverter when its DC or AC currents exceed 1.5 to 1.8 times nominal values [23].

IV. Complete Powertrain Simulation

After standalone modeling of all the components, a MATLAB/SIMULINK model of the entire powertrain is developed. In this model, the properties of all the components can be adjusted by the user, and different cases, including nominal flight scenarios and short circuit events, can be studied. This work analyzes a simulation flight scenario based on the motor speed variations and a 100 ms DC pole-to-pole short circuit at t=1.2 s with fault resistance of 1 mΩ between the DC cable and DC/AC inverter as shown in Fig. 1.

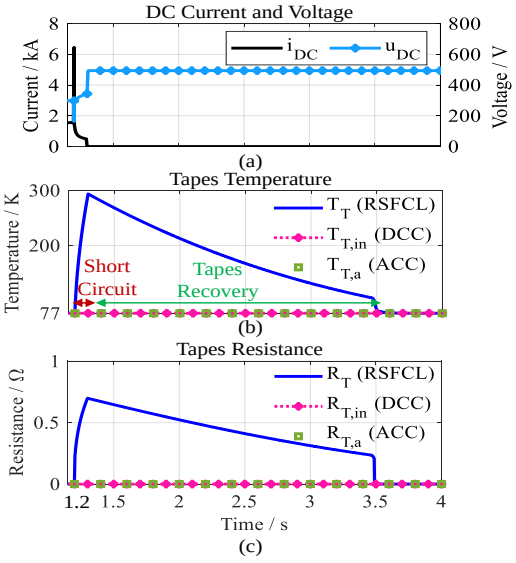

Fig. 7. DC pole-to-pole short circuit simulation results: (a) DC current and voltage on the fuel cell output, (b) tapes temperature, as T_{T} (RSFLC), $T_{\mathrm{T,in}}$ (DCC), and $T_{\mathrm{T,a}}$ (ACC) being the tapes temperature in the RSFCL, DC cable (DCC) inner pole, and phase a of the AC cable (ACC), (c) total tapes resistance, following the same naming style as tapes temperature.

In the simulation flight scenarios from takeoff to cruising and finally landing, the reference speed $n_{\mathrm{m,ref}}$ varies between 0 rpm to 1043 rpm. The simulation results are displayed in Fig. 6, showing that the main design parameters described in TABLE I are met. This figure highlights the fast and precise tracking of the reference speed by the PMSM control, with minimal transient error. Additionally, Fig. 6(c) depicts the fuel cell non-linear and dynamic response to the current variations.

In the case of the above-mentioned short circuit, the simulation results are depicted in Fig. 7. These results indicate the RSFCL proper design to limit the fault current and protect other components, particularly the DC and AC cables. Given that a lumped-parameter, non-adiabatic model is used for the RSFCL, the LN_2 absorbs the heat generated in the tapes, leading into their recovery to the superconducting state in approximately 2.3 s.

V. Conclusions

A hydrogen-powered electric aircraft with a superconducting powertrain presents a promising solution for decarbonizing aviation. Alongside the previous work [8], this work provides advanced modeling tools for such a powertrain. The main advantage is the ability to simulate the entire powertrain under various conditions without requiring separate models, enabling the users to customize component properties. Additionally, multiple models are available for most components, allowing users to select the ones that best suit their specific study case and requirements in any power system. Beyond high accuracy, these models are highly time-efficient, with the complete powertrain simulation for the 6 s simulation flight scenarios taking less than 3 minutes on a computer with a 6-core 2.3 MHz CPU and 16 GB RAM.

REFERENCES

[1] Z. Wang and Y. Bai, "Prediction of International Aviation Carbon Emissions and Offsetting Based on ICAO Mechanisms," *2023 5th International Conference on Power and Energy Technology, ICPET 2023*, pp. 1349–1353, 2023, doi: 10.1109/ICPET59380.2023.10367631.

[2] M. Klöwer, M. R. Allen, D. S. Lee, S. R. Proud, L. Gallagher, and A. Skowron, "Quan-tifying aviation's contribution to global warming," *Environmental Research Letters*, vol. 16, no. 10, Art. no. 104027, Nov. 2021, doi: 10.1088/1748-9326/AC286E.

[3] B. Graver, D. Rutherford, and S. Zheng, "CO2 Emissions from Commercial Aviation 2013, 2018, and 2019," 2020.

[4] Airbus, "Global Market Forecast," Jun. 2023, [Online]. Available: https://www.airbus.com/en/products-services/commercial-aircraft/market/global-market-forecast.

[5] S. Tiwari, M. J. Pekris, and J. J. Doherty, "A review of liquid hydrogen aircraft and propulsion technologies," *Int J Hydrogen Energy*, vol. 57, pp. 1174–1196, Feb. 2024, doi: 10.1016/J.IJHYDENE.2023.12.263.

[6] Airbus, "ZEROe - Towards the world's first hydrogen-powered commercial aircraft." [Online]. Available: https://www.airbus.com/en/innovation/energy-transition/hydrogen/zeroe.

[7] F. Berg, J. Palmer, P. Miller, and G. Dodds, "HTS System and Component Targets for a Distributed Aircraft Propulsion System," *IEEE Transactions on Applied Superconductivity*, vol. 27, no. 4, Jun. 2017, doi: 10.1109/TASC.2017.2652319.

[8] A. Khonya, M. Noe, W. T. B. D. Sousa, F. Berg, and M. Cooper, "Modeling Superconducting Components of the Electric Aircraft," *IEEE Transactions on Applied Superconductivity*, vol. 34, no. 3, pp. 1–5, May 2024, doi: 10.1109/TASC.2024.3350599.

[9] J. Larminie and A. Dicks, "Fuel cell systems explained: Second edition," pp. 1–406, Dec. 2013, doi: 10.1002/9781118878330.

[10] S. Chaudhary and Y. K. Chauhan, "Studies and performance investigations on fuel cells," *2014 International Conference on Advances in Engineering and Technology Research, ICAETR 2014*, 2014, doi: 10.1109/ICAETR.2014.7012957.

[11] N. Dyantyi, A. Parsons, C. Sita, and S. Pasupathi, "PEMFC for aeronautic applications: A review on the durability aspects," *Open Engineering*, vol. 7, no. 1, pp. 287–302, Feb. 2017, doi: 10.1515/ENG-2017-0035/ASSET/GRAPHIC/J_ENG-2017-0035_FIG_010.JPG.

[12] X. Qingshan, W. Nianchun, K. Ichiyanagi, and K. Yukita, "PEM fuel cell modeling and parameter influences of performance evaluation," *3rd International Conference on Deregulation and Restructuring and Power Technologies, DRPT 2008*, pp. 2827–2832, 2008, doi: 10.1109/DRPT.2008.4523891.

[13] J. M. Corrêa, F. A. Farret, V. A. Popov, and M. G. Simões, "Sensitivity analysis of the modeling parameters used in simulation of proton exchange membrane fuel cells," *IEEE Transactions on Energy Conversion*, vol. 20, no. 1, pp. 211–218, Mar. 2005, doi: 10.1109/TEC.2004.842382.

[14] E. J. F. Dickinson et al., "Modelling and validation of Proton exchange membrane fuel cell (PEMFC)," *IOP Conf Ser Mater Sci Eng*, vol. 290, no. 1, Art. no. 012026, Jan. 2018, doi: 10.1088/1757-899X/290/1/012026.

[15] W. Y. Chang, "Equivalent circuit parameters estimation for PEM fuel cell using RBF neural network and enhanced particle swarm optimization," *Math Probl Eng*, vol. 2013, Art. no. 672681, 2013, doi: 10.1155/2013/672681.

[16] W. Niu, K. Song, Q. Xiao, M. Behrendt, A. Albers, and T. Zhang, "Transparency of a Geographically Distributed Test Platform for Fuel Cell Electric Vehicle Powertrain Sy-stems Based on X-in-the-Loop Approach," *Energies 2018*, vol. 11, no. 9, Art. no. 2411, Sep. 2018, doi: 10.3390/EN11092411.

[17] F. Z. Belhaj, H. El Fadil, Z. El Idrissi, A. Intidam, M. Koundi, and F. Giri, "New Equi-valent Electrical Model of a Fuel Cell and Comparative Study of Several Existing Mo-dels with Experimental Data from the PEMFC Nexa 1200 W," *Micromachines 2021*, vol. 12, no. 9, Art. no. 1047, Aug. 2021, doi: 10.3390/MI12091047.

[18] M. Haidoury, A. El Fatimi, H. Jbari, and M. Rachidi, "Design of a Boost DC/DC Converter Controlling a Fuel Cell System Under Proteus," *2022 International Conference on Microelectronics, ICM 2022*, pp. 46–49, 2022, doi: 10.1109/ICM56065.2022.10005332.

[19] N. Rifai, J. Sabor, and C. Alaoui, "PEM Fuel Cell Dynamic Modeling Based On Transfer Functions," *2022 2nd International Conference on Innovative Research in Applied Science, Engineering and Technology, IRASET 2022*, 2022, doi: 10.1109/IRASET52964.2022.9738273.

[20] M. Raceanu, A. Marinoiu, M. Culcer, M. Varlam, and N. Bizon, "Preventing reactant starvation of a 5 kW PEM fuel cell stack during sudden load change," *Proceedings of the 2014 6th International Conference on Electronics, Computers and Artificial Intelligence*, ECAI 2014, pp. 55–60, 2014, doi: 10.1109/ECAI.2014.7090147.

[21] H. Ghanayem, M. Alathamneh, and R. M. Nelms, "PMSM Field-Oriented Control with Independent Speed and Flux Controllers for Continuous Operation under Open-Circuit Fault at Light Load Conditions," *Energies 2024*, vol. 17, no. 3, Art. no. 593, Jan. 2024, doi: 10.3390/EN17030593.

[22] P. Krause, O. Wasynczuk, S. Sudhoff, and S. Pekarek, *Analysis of Electric Machinery and Drive Systems*. Piscatawy, NJ: Wiley-IEEE Press, 2013.

[23] A. Khonya, "AC-DC Converters for Medium Voltage Direct Current Networks with Integrated Renewable Energy Sources," Master's Thesis, Politecnico di Milano, Milan, 2021. [Online]. Available: https://www.politesi.polimi.it/handle/10589/174884.